



Hydroxide Ion Conducting Viologen-Bakelite Organic Frameworks for Flexible Solid-State Zinc-Air Battery Applications

Journal:	<i>Nanoscale Horizons</i>
Manuscript ID	NH-COM-09-2022-000455.R1
Article Type:	Communication
Date Submitted by the Author:	23-Nov-2022
Complete List of Authors:	Rase, Deepak; IISER Pune, Chemistry Illathvalappil, Rajith; CSIR-National Chemical Laboratory, Physical and Materials Chemistry Singh, Himan; IISER Pune, Chemistry; IISER Pune, Chemistry Shekhar, Pragalb; IISER Pune, Chemistry Leo, Liya; IISER Pune, Chemistry Chakraborty, Debanjan; Indian Institute of Science Education Research Pune, CHEMISTRY; Halder, Sattwick; IISER Pune, Chemistry Shelke, Ankita; CSIR-National Chemical Laboratory, Physical and Materials Chemistry Division Ajithkumar, Thalasseril; CSIR-National Chemical Laboratory, Physical and Materials Chemistry Ramanathan, Vaidhyanathan; IISER Pune, Chemistry

In metal-air batteries, the hydroxide ions produced at the cathode by the reduction of oxygen from the air need to be efficiently transported to combine with the metal ions generated by the anodic oxidation. A liquid electrolyte like $\text{KOH}_{(aq)}$ typically transports ions. They suffer from drying up of the solvent over time; KOH is gellified to minimize this. However, in the gel, the electrostatic interaction between the K^+ and the OH^- restricts the facile movement of the latter. Also, a passivating layer of K_2CO_3 forms on the anode surface, creating internal resistance. To overcome this, we developed a cationic polymer with counter-balancing OH^- ions in their nanopores. The advantages are many. For example, the polymer is a steady source of OH^- ions since they are in a stoichiometric ratio with the cationic sites. There is no major solvent dependence- fewer problems with electrolyte drying up. Minimal use of KOH avoids the K_2CO_3 formation. Our insoluble polymer is a safe and humidity-withstanding solid-state electrolyte. This cationic polymer transports OH^- ions effortlessly and prevents undesirable cross-over of Zn^{2+} ions yielding high power density. Also, this bulk cationic framework does not compete with the hydroxide-ion diffusion during the operation, which lowers internal resistance.

ARTICLE

Hydroxide Ion Conducting Viologen-Bakelite Organic Frameworks for Flexible Solid-State Zinc-Air Battery Applications

Received 00th January 20xx,
Accepted 00th January 20xx

DOI: 10.1039/x0xx00000x

Deepak Rase,^{a,b†} Rajith Illathvalappil,^{a,b†} Himan Dev Singh,^{a,b} Pragalb Shekhar,^{a,b} Liya S Leo,^{a,b} Debanjan Chakraborty,^a Sattwick Haldar,^{a,b} Ankita Shelke,^c Thalasseril G. Ajithkumar^c and Ramanathan Vaidhyathan^{*a,b}

Adaptable polymer-based solid-state electrolytes can be a game-changer to safe, lightweight flexible batteries. We present a robust Bakelite-type organic polymer covalently decked with viologen, triazine, and phenolic moieties. Its flexible structure with cationic viologen centers incorporates counter-balancing free hydroxide ions into the polymeric framework. By design, the aromatic groups and the heteroatoms in the framework can be activated under an applied potential to prompt a push-pull drive setting off the towing of hydroxide ions through weak electrostatic, Vander Waals, and hydrogen-bond interactions. The frontier orbitals from a DFT-modeled structure certifies this. The hydroxyl-polymer requires minimal KOH wetting to maintain a humid environment for a Grotthuss type transport. The hydroxide-ion conductivity reaches a value of 1.4×10^{-2} S/cm at 80 °C and 95% RH, which is retained for over 15 h. We enhance its practical utility by coating it as a thin solid-state separator-cum-electrolyte on readily available filter paper. The composite exhibits a conductivity of 4.5×10^{-3} S/cm at 80 °C and 95% RH. A Zinc-air battery (ZAB) constructed using this polymer-coated paper as electrolyte yields a maximum power density of 115 mW/cm² and a high specific capacitance of 435 mAh/g. The power density recorded for our ZAB is among the best-performing polymer electrolyte-based ones. Subsequently, the flexible battery fabricated with IISERP-POF11_OH@FilterPaper shows an OCV of 1.44 V, and three batteries in series power a demo traffic signal. To underscore the efficiency of the hydroxide ions transport through the complex multi-functional backbone of the polymer, we have calculated the diffusion coefficient for the OH⁻ (Exp: 2.9×10^{-5} cm²/s; Comp. 5.2×10^{-6} cm²/s) using electrochemical methods and MD simulations. The climbing-edge NEB calculations reveal a large energy barrier of 2.11 eV for the Zn²⁺ to penetrate the polymer and identify the hydroxide ions within the polymer, suggesting no undesirable Zn²⁺ cross-over. Our findings assert readily accessible C-C-linked cationic polymer's capacity as solid-state electrolytes for ZAB and any anion conducting membrane.

Introduction

Hydroxide ion-conducting materials are receiving substantial attention owing to their significance in green technologies like anion exchange membrane fuel cells (AEMFCs), Metal-air batteries and water electrolyzers.¹⁻³ Typically, hydroxide ions exhibit low conductivity compared to the protons due to their sluggish diffusion and higher mass.⁴ Also, the proton-conducting materials are well established and commercialized for various energy applications.⁵⁻⁷ In comparison, the hydroxide ion-conducting materials are still in the infancy stage. Hence, the rational design of hydroxide ion-conducting materials is beneficial and would pave the way for application specific charge-storage devices.

The rapid increase in the energy requirement provides ample attention to the charge storage devices.⁸⁻⁹ In order to manage the everlasting energy demand, it is necessary to develop efficient and cost-effective charge storage devices.¹⁰⁻¹¹ In this regard, Zinc-air batteries (ZABs) are getting wide attention due to their high energy density, low cost and safe nature and, have been used for many applications like hearing-aid devices, cameras, grid-scale energy storage, etc.¹²⁻¹⁵ Development of high-performing ZABs requires the advancement of the electrodes and the separator.¹⁶⁻¹⁷ Along with the electrode kinetics, the hydroxide ion transport through the electrolyte largely determines the efficiency of ZABs.¹⁸ The liquid-based electrolytes create complications in fabricating or handling the devices and achieving a long cycle life.¹⁹⁻²⁰ In comparison, the solid-state electrolytes give less trouble in these regards and their leakage-proof framework offers superior safety features.²¹ Therefore, developing ZAB with solid-state separators and concomitantly possessing improved performance and flexibility would benefit applications.²² However, the key bottleneck associated with the hydroxide ion-conducting materials is their

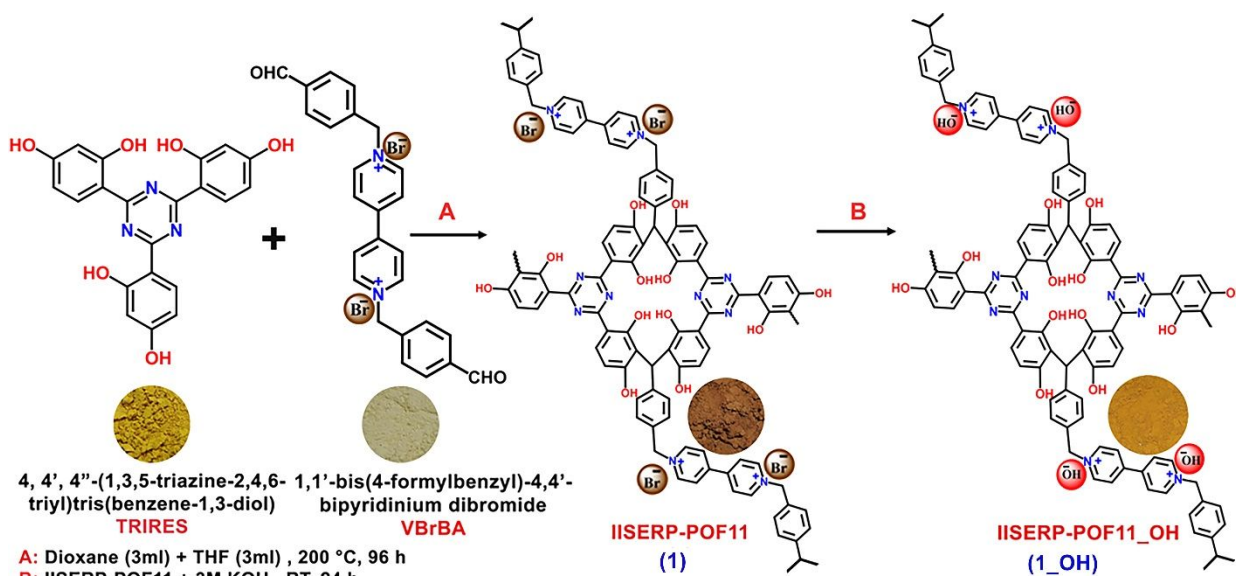
^a Department of Chemistry, Indian Institute of Science Education and Research, Dr. Homi Bhabha Road, Pashan, Pune 411008, India.

^b Centre for Energy Science, Indian Institute of Science Education and Research, Dr. Homi Bhabha Road, Pashan, Pune 411008, India.

^c Central NMR Facility and Physical/Materials Chemistry Division, CSIR-National Chemical Laboratory, Dr. Homi Bhabha Road, Pune 411008, India.

[†] D.R and R.I contributed equally to this work.

Electronic Supplementary Information (ESI) available: [details of any supplementary information available should be included here]. See DOI: 10.1039/x0xx00000x



Scheme 1: Synthetic procedure of **1_OH**. Insets show the photographic images of the corresponding compounds.

low ionic conductivity and poor stability under harsh chemical environments.²³ Several ion-conducting (H^+ or OH^-) materials with better conductivity have been reported in the pelletized state, but their practical potential as a thin and free-standing solid-state separator is not explored.^{4,24-27} Hence, we developed a thin hydroxide ion-conducting solid-state separator-cum-electrolyte for ZAB from the cationic polymer by coating it on filter paper (FP) adopting a simple dip-coating strategy.

Various kinds of separators have been employed for ZABs to transport OH^- ions and some porous separators provide satisfactory battery performance.^{14,28} A fundamental issue associated with the porous separators is the passage of zincate ions ($Zn(OH)_4^{2-}$) through the pores.²⁹ For example, the Celgard separators have good chemical stability and low cost. However, the significant transport of zincate ions from the anode to the cathode through the porous separator does happen, resulting in performance loss during the ZAB operation. One can overcome this by integrating the porous separators with the hydroxide ion-conducting insoluble materials. This would block the pores, allow the passage of OH^- ions, and restrict the movement of zincate ions.³⁰ Polymers are being intensely probed for their stability advantage,³¹ and recently, amide polymers constructed from simple monomers (acyl chloride + melamine) were shown to possess strengths comparable to steel.³² This inspired us to explore the potential of simple systems such as Bakelite and viologen for this task-specific application. Towards this approach, we have synthesized triazine-resorcinol and viologen-based cationic polymeric organic frameworks (POFs) with enriched hydroxyl ($-OH$) groups.³³ These POFs can be obtained in a large scale via a one-pot synthesis using Bakelite chemistry: forming robust C–C bonds without any catalyst.³⁴ Such types of POFs are chemically robust, thermally stable and find use in a wide range of applications, including energy storage, gas storage, catalysis, and anion exchange.³⁵⁻³⁸ The viologen-based quaternary center is counterbalanced by the larger anion like

Br^- which finds easy exchange with OH^- ions. Recently, our group reported a family of cationic POFs, amongst which IISERP-POF11 (**1**) performed excellently for the anion exchange.³⁸ Therefore, in the present work, hydroxide ion-exchanged IISERP-POF11, IISERP-POF11_OH (**1_OH**), was integrated with cellulose paper (IISERP-POF11_OH@Filter Paper, **1_OH@FP**) and employed as the solid-state separator-cum-electrolyte for Zinc-air battery applications. The integrated system displayed an improved performance for the ZAB and validated the suitability of employing **1_OH** for energy applications.

Results and discussion

Synthesis and bulk characterizations of as-made IISERP-POF11 (**1**) and hydroxide exchanged IISERP-POF11_OH (**1_OH**)

The synthesis of **1** from the monomers and its further conversion into **1_OH** after the exchange of the Br^- with OH^- ions is illustrated in Scheme 1 (detailed synthesis procedure is provided in the ESIT). The formation of as-synthesized polymer was confirmed by the various characterization techniques such as NMR, FTIR, FESEM, HRTEM, TGA, and N_2 adsorption viologen-measurements. The ^{13}C cross-polarization (CP) magic angle spinning (MAS) solid state Nuclear Magnetic Resonance (NMR) indicates the presence of Bakelite type coupling between triazine-resorcinol and viologen-based bipyridinium aldehyde (Fig. 1a), along with some unsubstituted sites on the phloroglucinol rings led to the formation of a characteristic aliphatic C–C bond which was observed around 26 ppm (a).³⁹⁻⁴¹ It was followed by the other characteristics peaks from aromatic groups like triazine around 172 ppm (i) and aromatic peak for based unit around 151 ppm (h). The aliphatic peaks for building blocks around 65 ppm (b) were intact. While this displays the polymerization taking place, to confirm the stability of the polymer powder, we recorded the IR and NMR spectrum of the material subjected to boiling in THF+DMF

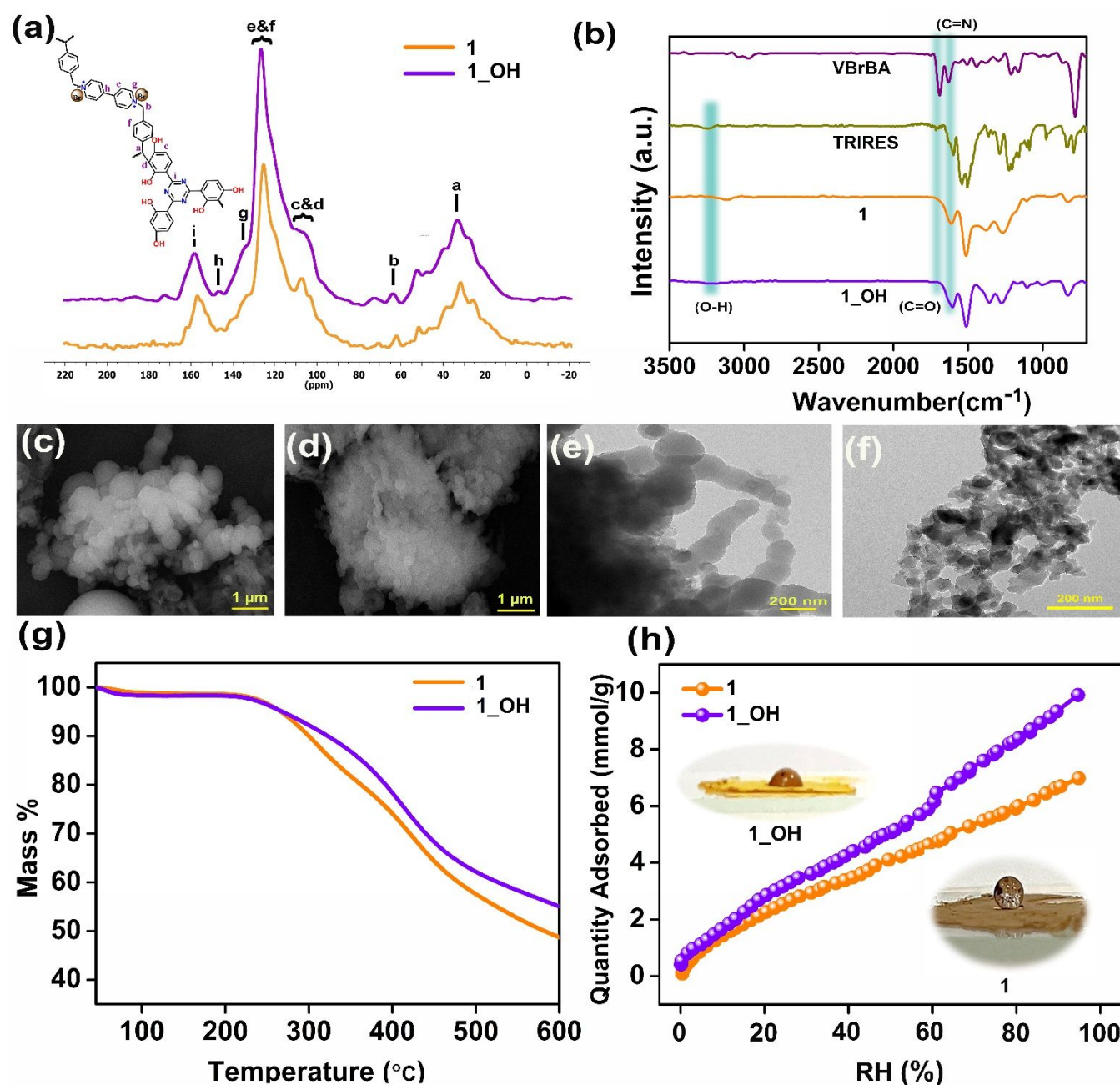


Fig. 1. (a) ^{13}C -CPMAS spectra of **1** and **1_{OH}**, (b) IR spectra of TRIRES, VBrBA, **1**, and **1_{OH}**, (c, d) FESEM images of **1** and **1_{OH}**, (e, f) HRTEM images of **1** and **1_{OH}**, (g) Thermogravimetric analysis of the **1** and **1_{OH}** under N_2 atmosphere at a ramp rate of $5^\circ\text{C}/\text{min}$ and (h) Water adsorption isotherms of **1** and **1_{OH}** with insets showing the photographic images from contact angle measurements.

mixture, followed by a 24 h soak in 6 M KOH solution. All the characteristic peaks remain and are positioned at similar chemical shifts with matching intensity. This exceptional chemical stability, and functional group integrity of the polymer especially towards harsh treatments is highly desirable for electrolyte applications (Fig. S1, ESI[†]). Subsequent to the anion exchange (Br with OH^- ions), a significant colour change from brown to yellow was observed and is represented with the photographic images in Scheme 1. The Fig. 1b shows the comparative IR spectrum of the monomers i.e., 1,1'-bis(4-formylbenzyl)-4,4'-bipyridiniumdibromide (VBrBA), 4,4',4''-(1,3,5-triazine-2,4,6-

triy)tris(benzene-1,3-diol) (TRIRES), as-synthesized cationic polymer (**1**), its hydroxide exchanged form, **1_{OH}**. The disappearance of the $\text{C}=\text{O}$ (1690 cm^{-1}) from the monomer VBrBA with the polymerization confirms the C-C bond formation between the aldehyde and the phenolic moieties (Scheme 1). Also, the presence of $\text{C}=\text{N}$ (1620 cm^{-1}) assures that the building blocks are intact in **1** and **1_{OH}** (Fig. 1b). The field emission scanning electron microscopy (FESEM) images of **1** indicate that the particles are connected or intergrown microspheres of different diameters ranging from 500 nm to 2 μm (Fig. 1c and Fig. S2, ESI[†]). It is confirmed from Fig. 1d and Fig. S3 that there is no deformation in the shape of these

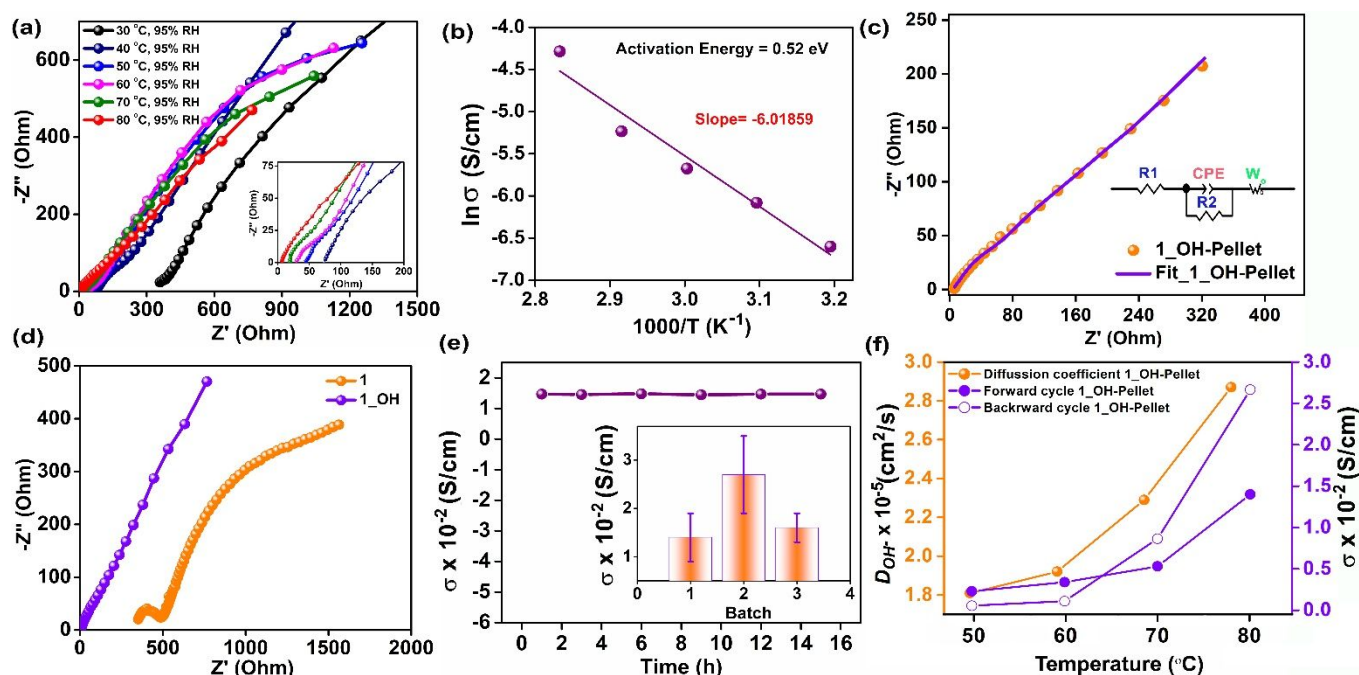


Fig. 2. (a) Nyquist plots from the temperature dependent conductivity measurements of **1_OH** and the inset shows its zoomed-in view, (b) Arrhenius plot of **1_OH**, (c) An equivalent circuit fit to the Nyquist plot of **1_OH** at 80 °C and 95% RH, (d) Comparison of the Nyquist plots of **1** containing Br⁻ as the counter ion vs. **1_OH**, (e) Conductivity of **1_OH** at 80 °C and 95% RH recorded for 15 h, inset shows the conductivity is reproducible across different batches of the sample, (f) Hydroxide ion diffusion coefficient and forward-backward cycling plot for OH⁻ conductivity of **1_OH** at different temperatures and a constant relative humidity of 95%.

microspheres after treating with 3 M KOH solution, i.e., on the formation of **1_OH**. This indicates their textural stability under the harsh corrosive environment. Thus, **1_OH** could be suited for operating under concentrated alkaline conditions. In the Energy dispersive X-ray (EDX) analysis, the drop in the atomic percentage of Br⁻ ions from 1.74 to 0.21% confirms the effective exchange of Br⁻ ions with OH⁻ to form **1_OH** (Fig. S4-S5, ESI[†]). The K⁺ ion traces in **1_OH** is negligible, which confirms that the hydroxide ions are counter-balanced by the cationic centers of the polymer. The High-resolution transmission electron microscopy (HRTEM) images of **1** and **1_OH** are displayed in Fig. 1e and Fig. 1f, respectively. The HRTEM showed that the spherical balls in **1_OH** are connected incessantly, which could aid the ionic transport across grains and spheres. After OH⁻ ion exchange, we noticed a slight decrease in the surface diameter of **1_OH** spheres and this could be due to more compacting from OH⁻ compared to Br⁻. However, the spherical morphology is still intact (Fig. S6-S7, ESI[†]).

Thermogravimetric analysis in Fig. 1g revealed that the framework **1** is stable up to 280 °C. We attribute this to the strong C-C bond formed between the monomers, resembling Bakelite. The cationic polymer treated with 3 M (**1_OH**) and 6 M KOH (**1_6OH**) display slightly different TGA profiles (Fig. 1g and Fig. S8a, ESI[†]), but their thermal stabilities are comparable. The contact angle measurements pointed at the surface of the as-made polymer powder, **1** being superhydrophobic; however, the **1_OH** prepared by anion exchange in an aqueous alkaline solution yielded a final powder that was hydrophilic (Fig. 1h and Fig. S8b-S8c, ESI[†]). This surface wettability is crucial for the material's interaction with

electrolytes. We investigated the intrinsic porosity with water sorption isotherms. The water adsorption isotherms of **1** and **1_OH** showed a very similar profile stating that there were no major changes to the pore environment or structure. The overall water capacity of the **1_OH** is higher than **1**, suggesting improved intrinsic wettability. Thus, the near superhydrophobic ($148^\circ \pm 3^\circ$) material with Br⁻ containing framework becomes much more hydrophilic when exchanged with OH⁻. Notably, there was no noticeable swelling of the polymer or significant change in density.

The density functional theory-based model fitted to the 77 K N₂ isotherm shows the majority of the pores being 15 to 18 Å in size, which are still intact after the ion exchange (Fig. S9, ESI[†]). However, the N₂ uptakes are nominal, which is expected as the pores are permanently occupied by the counterbalancing anions. Still, there is sufficient openness to support the transport of OH⁻ ions; also, unlike the crystalline frameworks, these polymers can exhibit structural flexibility with changing humidity, opening up spaces for dynamic interactions between the framework atoms and the free hydroxide ions. This impacts the electrolyte's wetting and hydroxide ion transport characteristics (Fig. 1h).

Electrochemical studies

Electrochemical impedance analysis was performed in the frequency range of 10⁶ to 0.1 Hz with an AC amplitude of 10 mV using Solartron impedance analyzer. The impedance was recorded at variable temperatures from 30 °C to 80 °C with a constant relative humidity of 95 % and the data is presented as Fig. 2a. To evaluate the intrinsic conductivity of the **1_OH**, the measurements were performed on a densely pressed pellet of

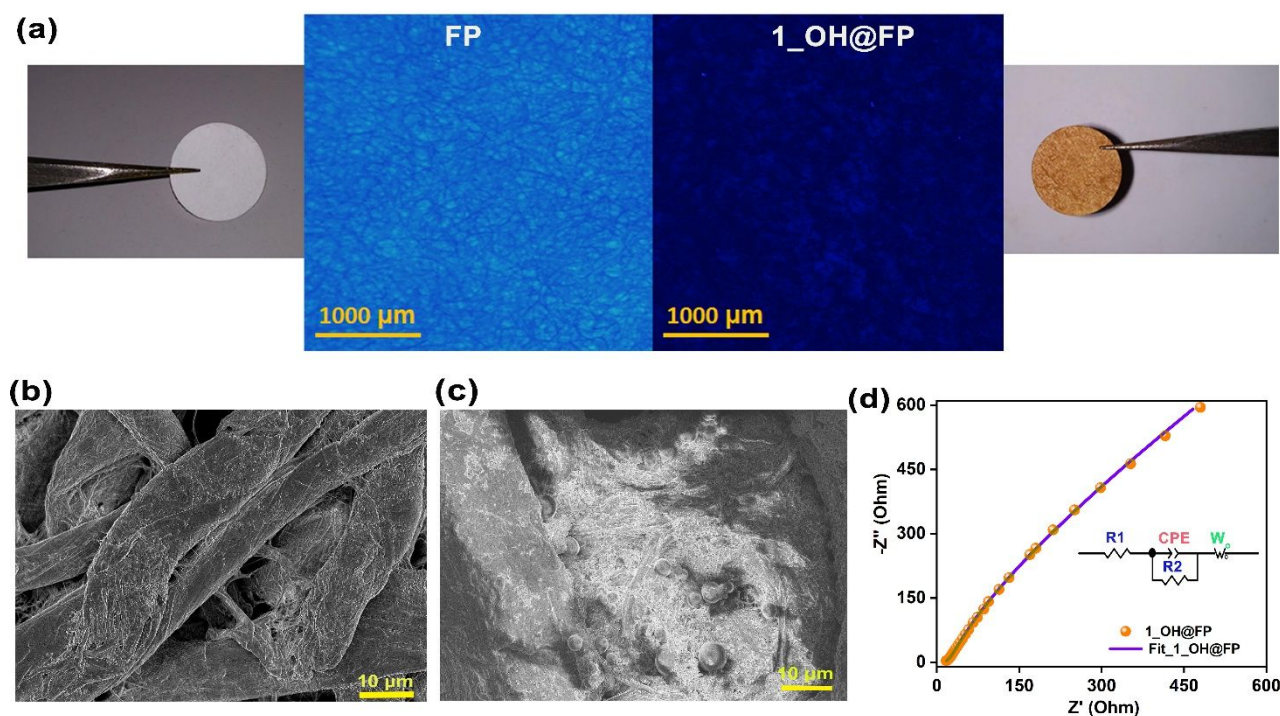


Fig. 3. (a) Macro zoom fluorescence microscope images of neat FP and 1_OH@FP with side-on images showing the corresponding photographic images, (b, c) FESEM image of neat FP and 1_OH@FP, (d) An equivalent circuit fit to the Nyquist plot of 1_OH@FP at 80 °C and 95% RH.

the same. The equivalent circuit was employed for fitting all the Nyquist curves, using the Zview-4 software. At a constant relative humidity of 95 %, the OH⁻ ion conductivity value increases from 2.7×10^{-4} S/cm at 30 °C to 1.4×10^{-2} S/cm at 80 °C (Fig. 2a and Table S1, ESI[†]). In order to check the humidity dependent conductivity of **1_OH**, we measured ac-impedance at 80 °C by varying the humidity (60% RH, 80% RH and 95% RH) (Fig. S10a, ESI[†]). The conductivity values are 3.6×10^{-5} , 3.8×10^{-4} and 1.4×10^{-2} S/cm at RH of 60%, 80% and 95%, respectively. The increase in hydroxide ion conductivity at 80 °C with increasing temperature suggests lowering of activation energy, while the increase in conductivity with increasing humidity suggests water could be playing a crucial role via hydrogen bonding.⁴² Fitting an Arrhenius equation to this temperature-dependent impedance data yields an activation energy of 0.52 eV (Fig. 2b) suggesting a mixed Grotthuss-Vehicular diffusion mechanism.⁴³ The observed activation energy is comparable to some of those reported for hydroxide ion in other nanoporous structures.⁴⁴ An equivalent circuit fit to the most promising Nyquist plots (80 °C, 95% RH) reveals an ohmic resistance of 3.2 Ω (neat pellet) (Fig. 2c). In the fitted equivalent circuit, we confirmed the need for a CPE component, by measuring the CV of the **1_OH**, which clearly indicated the capacitive behavior being present (Fig. S11, ESI[†]). In our case, considering that the hydroxide is moving in channels lined with hydroxyl groups and triazine, both of which might provide some hydrogen bond assistance resulting in Grotthuss mechanism, at the same time, under the applied ac-potential, there could be sufficient force for a vehicular motion too. Due to the absence of OH⁻ ions in the pristine polymer (**1**), it shows a poor ionic

conductivity value of 7.39×10^{-5} S/cm at 80 °C and 95% RH. This is expected as the Br⁻ ions are heavier and will be even less effective for a hydrogen-bond assisted Grotthuss type movement. Further, the comparison of the equivalent circuit fitted Nyquist plots of the **1** vs. **1_OH** (Fig. 2d) suggests that the series resistance and charge-transfer resistance both are substantially higher for the **1** ($R_1 = 352 \Omega$, $R_2 = 509 \Omega$) compared to the **1_OH** ($R_1 = 3.2 \Omega$, $R_2 = 11.8 \Omega$). The large semi-circle in the low-frequency regime in the case of **1** suggests limited or restricted diffusion even in the same time-scale of measurements as employed for the **1_OH**. Meanwhile **1_OH** has a typical semi-infinite linear diffusion – that is, diffusion in one dimension which is only bounded by a large planar electrode on one side (45° angle with Z'-axis), a typical Warburg behavior. A CPE-P value close to 0.5 for **1_OH** pellet is suggestive of a pseudocapacitive behaviour expected for the polymer with the porous structure (Fig. 2c). Remark: A transmission line model mimicking the Fickian diffusion, wherein the movement of ions through the pores is coupled to the movement of electrons through the pore walls, was not chosen. This is considering that the polymer does not have a crystalline structure with highly ordered pores and also the electronic conductivity in larger length scales is limited.⁴⁵ The linear sweep voltammetry (LSV) was conducted to check the electronic conductivity of **1_OH** in the potential window of -0.6 to 0.6 V with a scan rate of 10 mV/s (Fig. S12, ESI[†]). **1_OH** shows negligible electronic conductivity which suggests that the observed conductivity is predominantly ionic arising from the OH⁻ ions. To assess the ability of **1_OH** in delivering a stable hydroxide-ion conductivity, we measured it at 80 °C and 95 % RH for 15 h. There is a build-up of a small charge transfer

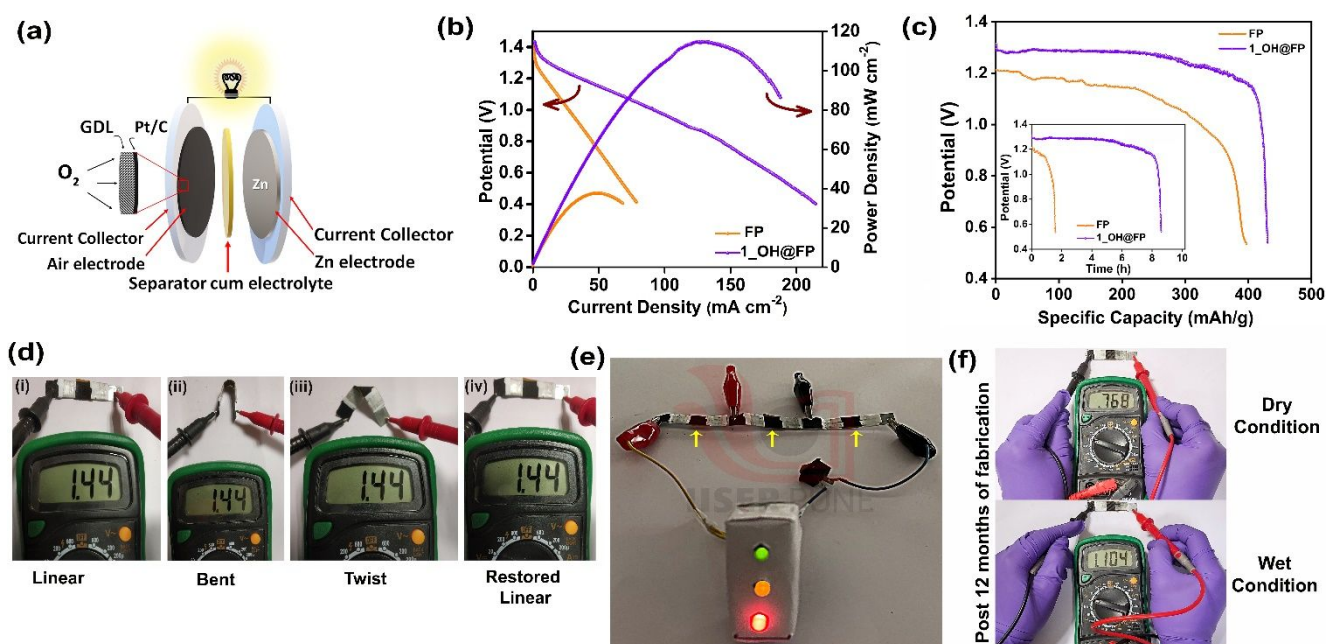


Fig. 4. (a) The schematic of the ZAB with its components, (b) Polarization plot of neat FP and $1_OH@FP$ based ZAB, (c) Comparative specific capacity of neat FP and $1_OH@FP$ based batteries, inset shows the durability of the ZAB over the time, (d) Photographic images showing constant OCV at different flexible modes of solid-state ZAB, (e) Image of the flexible solid-state ZAB powering a demo traffic signal with yellow arrows indicating the air-breathing cathode, (f) OCV regeneration of solid-state ZAB after 10 months of fabrication on wetting with water.

resistance over 15h, and notably, the 1_OH retains > 95% of its resistance over 15h, and notably, the 1_OH retains > 95% of its conductivity (Fig. 2e and Fig. S10b, ESI[†]). This hydroxide ion conductivity is reproducible across different batches of the sample (Fig. 2e inset). To check the cyclic stability of 1_OH for OH^- transport, the pellet was dried overnight at 100 °C in a vacuum oven, the impedance analysis was carried out for both the forward cycle (increasing the temperature from 30 to 80 °C at 95% RH) and the backward cycle (decreasing the temperature from 80 to 30 °C at 95% RH) (Fig. 2f). The conductivities remained the same during the cycling reflecting the electrochemical stability of the polymer and the shape/profile of the Nyquist plots remained alike suggesting that the pathway and the mechanism of conduction is unchanged. We calculated

the diffusion coefficient for the hydroxide ions inside the cationic polymer framework using the Z' vs. $\omega^{-1/2}$ plot. The low-frequency spectrum of the impedance plot yielded the characteristic linear fits (Fig. S13, ESI[†]) from which the diffusion coefficients were estimated to be $2.9 \times 10^{-5} \text{ cm}^2/\text{s}$ at 80 °C with 95% RH. The diffusion coefficient increases systematically with increase in temperature (Fig. 2f). The calculated diffusion coefficients match well with the theoretical values reported in the literature.⁴⁶⁻⁴⁷ However, we could not find any experimentally calculated diffusion coefficients for hydroxide ions inside a porous material, but for Cl^- the diffusion coefficient is of the order of $10^{-8} \text{ cm}^2/\text{s}$.⁴⁸

Conductivity characteristics of 1_OH coated on Filter Paper ($1_OH@FP$)

Encouraged by the appreciable hydroxide ion conductivity and stability exhibited by this viologen polymer, we set out to

investigate its scope as a solid-state electrolyte in a Zinc-air battery. It is hugely advantageous to coat the polymer on a porous filter paper, which provides a bulk wettable microporous-macroporous separator-cum-electrolyte membrane. However, the composite needs to retain the high levels of OH^- ion conductivity. To investigate this, the 1_OH was devised into a separator-cum-electrolyte by coating it on research-grade Whatman filter paper ($1_OH@FP$). Commonly available filter paper was chosen owing to its advantageous features such as low cost, lightweight, flexibility and easy accessibility.⁴⁹ The dip-coating method was used to deposit the polymer by soaking cellulose paper in a dispersed solution of 1_OH in water. The process is scalable and 25 cm^2 $1_OH@FP$ was prepared in a few hours. The fluorescence microscopy images illustrated in Fig. 3a shows the loss of fluorescence of the FP upon loading with the polymer. Its uniform loading on paper is evident. Typically, the filter paper has entangled cellulose fibres (Fig. 3b) which are rich-in terminally placed binding groups, which are likely to be compatible with our hydroxyl-functionalized polymer backbone. The solid-state UV-Vis absorption spectra of neat FP vs. $1_OH@FP$ showed lowering of the absorbance intensity (@280 nm) of the FP upon coating with the polymer (Fig. S14, ESI[†]), which is in agreement with the results from the fluorescence microscopy. These suggest the polymer directly contacting the electrolyte and the electrodes, while the paper is acting as a separator. From the FESEM images it is evident that the polymer composite buries extremely well into the cellulose matrix of the paper (Fig. 3b-3c and Fig. S15-S16, ESI[†]). This could be crucial to providing an intimate contact between the two entities in the composite. The cross-sectional SEM analysis of $1_OH@FP$ displayed the distribution of 1_OH is uniform in FP.

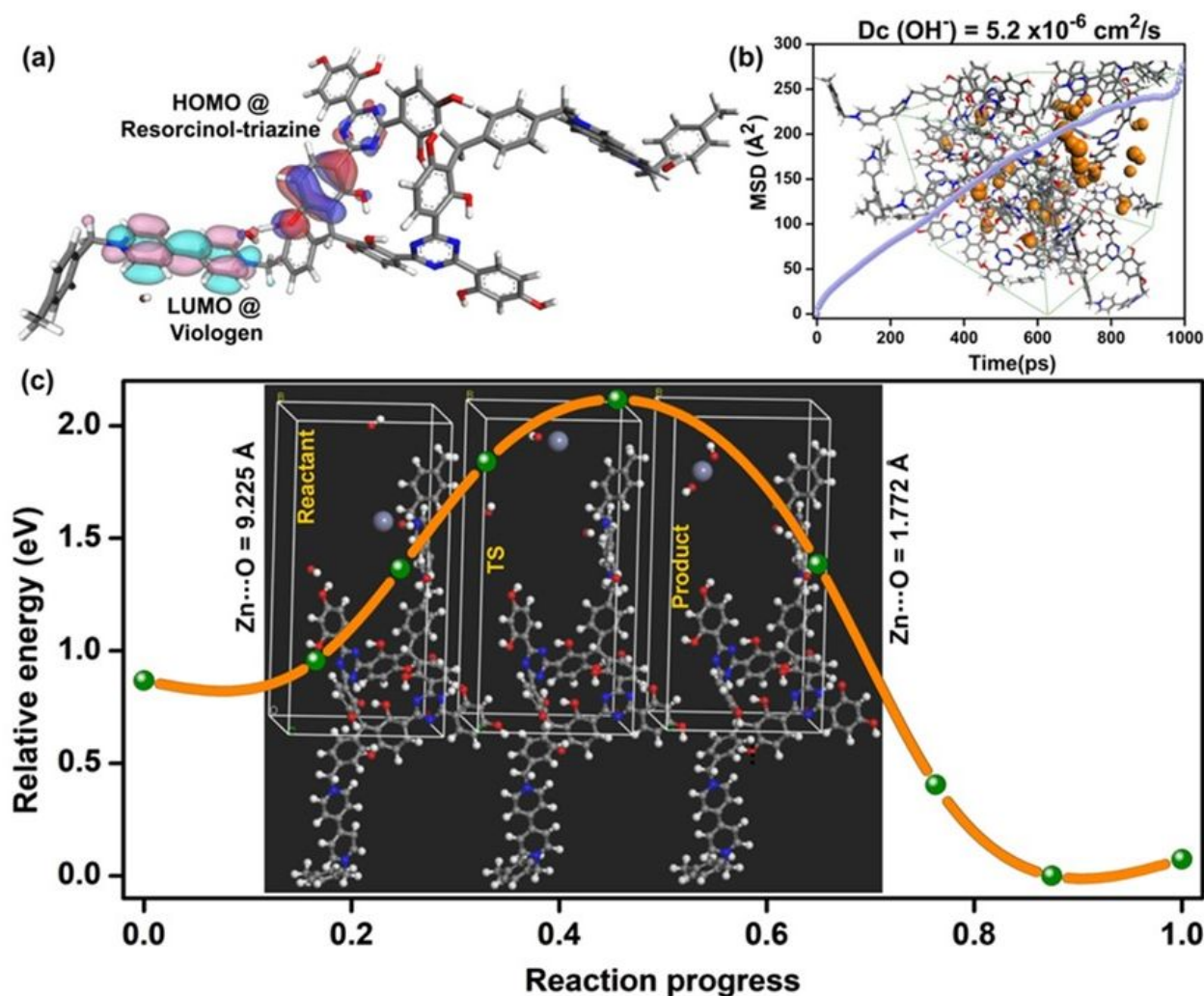


Fig. 5. Computational modeling: (a) Frontier orbital locations within the polymer backbone. The resorcinol-triazine could set-up a push-pull with the e- deficient viologen units. (b) Mean Square Displacement (MSD) vs. time plot calculated using MD simulations and the derived hydroxide ion self-diffusion coefficient. Inset shows the snapshot of an optimized structure with hydroxide ions shown as space fills. (c) A representative minimum energy path (MEP) for the Zn^{2+} ions movement within the hydroxyl-containing polymer assessed from NEB.

The fibers of the FP are intimately blended to good thickness (not merely coating the surface) with small granules of **1**_OH. (Fig. S16). Even a strong thumb-pressure does not make the polymer particles lose its adhesion with the paper. The hydroxide ion conductivity of **1**_OH@FP was analyzed at 80°C and 95 % RH and the Nyquist plot is presented as Fig. 3d and Fig. S17. **1**_OH@FP shows a OH^- conductivity value of 4.5×10^{-3} S/cm at 80°C and 95 % RH ($R_1 = 10.4$ and $R_2 = 18.2 \Omega$), which is quite comparable to the values obtained with the pellets at similar operating conditions. The same equivalent circuit fits extremely well. From the fitted data we observe the resistances of the **1**_OH@FP is relatively higher, which is expected as more interfaces are generated and the paper is much less conductive. Notably the CPE value of the **1**_OH (0.45) increases to 0.72 for the **1**_OH@FP indicating the increase in double layer capacitive character. Interestingly, the ion diffusion is noticeably improved when the material is coated on the FP (Fig. S18 ESI[†]). Comparing the Warburg tail of the **1**_OH pellet versus the **1**_OH@FP brings some noteworthy features. At lower frequencies, the diffusion tail of the

1_OH@FP starts to deviate more and more from making an angle of 45° with the x-axis, and this indicates deeper penetration of the ions into the material even at these low frequencies, which is expected as the active material is coated on a paper to form a much thinner electrolyte membrane compared to the pellet. This points at the advantage of making this paper-derived electrolyte-cum-separator unit. Importantly, the overall conductivity still remains very much in acceptable regime for a hydroxide-ion conducting electrolyte. Thus, the **1**_OH@FP provides an appropriate electrolyte material with micro-macroporous structure that still inhibits the direct zincate ion crossover through the separator, properties which are crucial for the battery performance.

1_OH@FP as solid-state electrolyte in ZAB

The excellent ionic conductivity of **1**_OH@FP fascinated us to use it for Zinc-air battery applications. For this, **1**_OH@FP was employed as the solid-state separator-cum-electrolyte by sandwiching between the electrodes. Fig. 4a depicts the

schematic of the Zinc-air battery assembly with its components (Fig. S19, ESI[†]). During discharge, oxygen electrocatalytically reduces to form hydroxide ions at the cathode.⁵⁰ At the anode, zinc would oxidize to Zn²⁺. The zinc ions would react with the hydroxide ions coming from the cathode through the separator to form zincate ions and further to ZnO. To assess the performance of **1_OH@FP** in ZAB, LSV was performed at a scan rate of 10 mV/s and shown in Fig. 4b. The polarization analysis presented in Fig. 4b shows a maximum power density of 115 mW/cm² for **1_OH@FP** based battery compared to 38 mW/cm² obtained for the neat filter paper-based counterpart. The resistances of the **1_OH@FP** vs. **neat FP** were determined from impedance analysis performed on their respective ZAB assemblies. The ohmic drop in **1_OH@FP** is notably lower compared with neat **FP** (1.55 vs. 2.1 Ω) (Fig. S20-S21, ESI[†]). Also, the resistance increases almost by 0.85 Ω during the use of the neat **FP** as electrolyte support in the battery which was run for about 2h. In contrast, the **1_OH@FP**, maintains almost the same resistance even after 8h under comparable battery set-up. It is worth mentioning that even a difference of 0.55 Ω (between **FP** vs **1_OH@FP**) hugely impacts the power density (Fig. 4b) as well as the run time of the ZAB derived out of these electrolyte supports. Accordingly, the **1_OH@FP** containing battery exhibits a higher specific capacitance of 435 mAh/g compared to 397 mAh/g obtained for the neat **FP** based battery. Also, the Fig. 4c inset shows that **1_OH@FP** containing battery delivers the four times more run time compared with **FP** based ZAB. Flexible solid-state ZAB was fabricated to show the practical applicability of the as-prepared **1_OH@FP** (details provided in the experimental section). The fabricated solid-state battery offers an OCV value of 1.44 V in an air atmosphere (without purging any additional O₂ gas). Three flexible devices connected in series yielded an output of 4.22 V (Fig. S22, ESI[†]). The output voltage was stable to bending and twisting (Fig. 4d) owing to the liquid-free nature of the **1_OH@FP**. By combining the batteries in series, we could power three light-emitting diodes (LEDs) connected in parallel, resembling the traffic signal lights (Fig. 4e). On top of that, after 12 months from the fabrication we were able to regenerate the OCV of 1.10 V on wetting the device with just 50 μL of water (Fig. 4f). Overall, the results indicate the feasibility of employing **1_OH@FP** as the hydroxide ion-conducting material for flexible batteries.

Post ZAB usage stability analysis of **1_OH@FP**

The stability **1_OH@FP** when employed as separator-cum-electrolyte in the ZAB was investigated. The PXRD and IR analysis indicated that the polymer remains intact on the FP even after the complete discharge cycle (8h) (Fig. S23- S24, ESI[†]). Then this composite electrolyte in the ZAB, **1_OH@FP**, was subjected to high-frequency impedance analysis after a complete discharge cycle and compared with the neat **FP**'s performance (Fig. S20-S21, ESI[†]). The resistance remains the same for the **1_OH@FP** but increases for the neat **FP**; this is due to the relatively higher loss of KOH (aqueous solution) from the neat **FP** creating a passivation layer disfavoring the

conduction. This problem is not observed in the case of the **1_OH@FP**. Most likely due to the intrinsic tendency of the polymer to hold on to OH⁻ species driven by its charge-balance requirements, and their pores trap water more efficiently (Fig. 1h). Also, in the case of **1_OH@FP**, the conduction pathway and diffusion mechanism remain the same as seen from the equivalent circuit fits. The post-ZAB microscopy analysis of the **1_OH@FP** further confirms the homogeneous adherence of the active material on the FP (Fig. S25-S26, ESI[†]).

Push-pull electronics in the triazine-resorcinol-viologen framework portrayed by frontier orbitals

To investigate the potential role of the cationic polymers in interacting with the hydroxide ion movement in this viologen functionalized spongy polymer, we looked at the potential/electron distribution within the polymer backbone. As a coherent step, we replaced the heteroatoms within the covalently linked modules and monitored the impact it brings to the HOMO-LUMO distribution. The local electronics is likely to be dictating the hydroxide-framework (heteroatom) interactions. For this, we developed a two-repeat unit polymer using the Random Copolymer module in the Materials Studio. This initial model was then geometry optimized using DMOL³ package.

The geometry optimizations were performed for each of the individual configurations that were generated with and without heteroatoms. Important demarcation arises from the position of the HOMO and the LUMO. The **1_OH** with conjugated triazine-resorcinol core covalently linked to the viologen units have the HOMO residing on the resorcinol ring and the triazine nitrogen and to some extent on the hydroxyl groups that are located proximal to the viologen (Fig. 5a). While the LUMO resides mostly on the viologen rings. For the as-made polymer the HOMO-LUMO gap turns out to be 0.03 eV, but when the triazine rings are replaced with phenyl moieties, the all-carbon backbone does not demarcate much between the HOMO-LUMO levels leading to a gap of 0.002 eV.

This removes the push-pull characteristics within the framework backbone. This points at how crucial the triazine nitrogens are in setting up the push-pull characteristics between the triazine-resorcinol unit and the viologen rings. Remark: This is only for the small section of the polymer, and as the polymer grows into amorphous extended cross-linked structure there is bound to be breakdown of long-range conjugation assisted electronic transport and the overall bandgap will be much larger, typically in the semiconducting regime.³¹ However, the redox active localized regions are sufficient to set-up a push-pull effect, which would govern the movement of the hydroxide ions.

Diffusion coefficient of hydroxide ions in the viologen polymer

We resorted to MD simulations for garnering insights into the transport of hydroxide ions within the polymer framework. All structural dynamics were carried out using the Forcite module in the Materials Studio. An amorphous cell was constructed for a structure encompassing cross-linked chains. These were filled with hydroxide ions in a 8:32 ratio per unit cell. A

rigorous geometry optimization was performed until excellent convergence was achieved. The optimized structure was further equilibrated using an NPT ensemble and the average lattice parameters were employed to output structure. The migration of the hydroxide ions in the cationic framework was explored under the NVT conditions and the final trajectory was obtained from a 1ns microcanonical NVE dynamics with a large 50Å cut-off distance performed at 300K. The Mean Square Displacement (MSD) vs time plots were used to calculate the average diffusion coefficient for the hydroxide ions, which turned out to be $5.2 \times 10^{-6} \text{ cm}^2/\text{s}$ (Fig. 5b). However, the computed diffusion coefficient is lower than the experimental one ($2.9 \times 10^{-5} \text{ cm}^2/\text{s}$), because the hydration was not considered in the MD simulations.⁵¹ Importantly, the observed and calculated diffusion coefficients for the hydroxide ions compare extremely well with those available from the recent computational works.⁵²⁻⁵⁵ From the fits to the MSD plots, we estimated the activation energy for the diffusion of the hydroxide ions in the cationic polymer framework to be 0.22 eV (21 kJ/mol, Fig. S27, ESI[†]), which is comparable to the experimental activation energy (0.153 eV) (14.77 kJ/mol) calculated using the Warburg Bode plot (Fig. S27, ESI[†]).⁵⁶

Large energy barrier for Zinc-ion incorporation into the cationic polymer

To estimate the energy barriers associated with the process of incorporation of the Zn^{2+} ions into the polymer and its interaction with the OH^- ion, we used the Nudged Elastic Band calculations. In the "reactant" model, the Zn^{2+} ions were positioned relatively farther from the hydroxide ions present within the polymer's unit cell. Meanwhile, we configured the "product" to have the Zn^{2+} ions at a bonding distance to the hydroxide ions (Fig. 5c). The framework atoms of the "reactant" and "product" were made indistinguishable to sequester only the effect of Zn-ion incorporation. Then a transition state confirmation for the bound state was performed using the climbing-image NEB method. We included multiple intermediate configurations between reactant-TS and TS-product to obtain a good extrapolation of the minimum energy path (MEP) and optimized under the NEB. The E_a for the Zn^{2+} ions incorporation was calculated using as much as 7 intermediate configurations.

Most importantly, both the reactants and the product configurations showed stable structure, and the incorporation of the Zn^{2+} ions go through an acceptable intermediate but with a significant energy barrier (2.11 eV). We observe that the energy barrier for incorporating zincate-ion into the polymer were even higher, and the zincate species goes through some unacceptable geometry deformations due to repulsive interactions with the polymer's framework atoms. This reveals the non-compatibility of the Zn^{2+} ions and zincates in the polymer, a desirable feature in preventing zinc-dendrimer formation or cell short-circuiting.

Conclusions

This work describes a cationic polymer with counter-balancing hydroxide anions as a solid-state electrolyte for a Zinc-air battery. The uniqueness of the work is its simplicity and yet delivering high performance. We couple Bakelite and viologen chemistry to make this polymer which is exceptionally stable, easy to make, and affordable. The organic nature of this ion-conducting polymer ($1.4 \times 10^{-2} \text{ S/cm}$ at 80 °C and 95% RH) integrates it well with filter paper to yield an electrolyte requiring minimal KOH wetting. **1_OH@FP** delivers an excellent performance as separator-cum-electrolyte for Zinc-air battery with a power density of 115 mW/cm², three times more than the neat filter paper-based counterpart. The fabricated device easily withstands bending and twisting operations. Gradual and constant increment in OCV was observed for devices upon connecting them in series, enabling them to light up a power-demanding traffic signal for a long time. Computational modeling reveals the importance of heteroatoms in providing an electronic push-pull across the framework, which aids in transporting the hydroxide ions. At the same time, the MD simulations confirm the favorable diffusion of hydroxide ions and the high barrier for the undesirable penetration of Zn^{2+} ions into the polymer. Thus, our findings assert readily accessible C-C-linked cationic polymer's capacity as solid-state electrolytes for ZAB and any anion conducting membrane.

Conflicts of interest

"There are no conflicts to declare".

Acknowledgements

We acknowledge IISER Pune for support and the funding by the "DST for material for energy storage (DST/TMD/MES/2k17/103), Air Force Office of Scientific Research under Award Number FA2386-21-1-4022, MHRD-STARS [STARS1/278] and SERB (CRG/2021/008250) program. We thank DST-Nanomission for technical support under the Thematic Unit Program (SR/NM/TP-13/2016). We thank biology microscopy facility, IISER Pune. D.R and R.I acknowledge IISER Pune and MHRD-STARS for financial support. We thank Dr. Sreekumar Kurungot, CSIR-NCL, Pune, for the materials support.

References

- 1 J. R. Varcoe, P. Atanassov, D. R. Dekel, A. M. Herring, M. A. Hickner, P. A. Kohl, A. R. Kucernak, W. E. Mustain, K. Nijmeijer, K. Scott, T. Xu, L. Zhuang, *Energy Environ., Sci.* 2014, **7**, 3135-3191.
- 2 N. Chen, H. H. Wang, S. P. Kim, H. M. Kim, W. H. Lee, C. Hu, J. Y. Bae, E. S. Sim, Y.-C. Chung, J.-H. Jang, S. J. Yoo, Y. Zhuang, Y. M. Lee, *Nat. Commun.*, 2021, **12**, 2367.
- 3 D. R. Dekel, *J. Power Sources*, 2018, **375**, 158-169.
- 4 S. Tao, H. Xu, Q. Xu, Y. Hijikata, Q. Jiang, S. Irle, D. Jiang, *J. Am. Chem. Soc.*, 2021, **143**, 8970-8975.
- 5 K.-D. Kreuer, *Chem. Mater.*, 1996, **8**, 610-641.

- 6 Y. Meng, J. Gao, Z. Zhao, J. Amoroso, J. Tong, K. S. Brinkman, *J. Mater. Sci.*, 2019, **54**, 9291-9312.
- 7 L. Malavasi, C. A. J. Fisher, M. S. Islam, *Chem. Soc. Rev.*, 2010, **39**, 4370-4387.
- 8 S. S. Shinde, C.-H. Lee, A. Sami, D.-H. Kim, S.-U. Lee, J.-H. Lee, *ACS nano*, 2017, **11**, 347-357.
- 9 Z. Li, W. Niu, Z. Yang, N. Zaman, W. Samarakoon, M. Wang, A. Kara, M. Lucero, M. V. Vyas, H. Cao, H. Zhou, G. E. Sterbinsky, Z. Feng, Y. Du, Y. Yang, *Energy Environ. Sci.*, 2020, **13**, 884-895.
- 10 S. Haldar, D. Kaleeswaran, D. Rase, K. Roy, S. Ogale, R. Vaidhyanathan, *Nanoscale Horiz.*, 2020, **5**, 1264-1273.
- 11 R. Kushwaha, S. Haldar, P. Shekhar, A. Krishnan, J. Saha, P. Hui, C. P. Vinod, C. Subramaniam, R. Vaidhyanathan, *Adv. Energy Mater.*, 2021, **11**, 2003626.
- 12 J. Fu, R. Liang, G. Liu, A. Yu, Z. Bai, L. Yang, Z. Chen, *Adv. Mater.*, 2019, **31**, 1805230.
- 13 W. Sun, F. Wang, B. Zhang, M. Zhang, V. Küpers, X. Ji, C. Theile, P. Bieker, K. Xu, C. Wang, *Science*, 2021, **371**, 46-51.
- 14 Y. Li, H. Dai, *Chem. Soc. Rev.*, 2014, **43**, 5257-5275.
- 15 Q. Liu, Y. Wang, L. Dai, J. Yao, *Adv. Mater.*, 2016, **28**, 3000-3006.
- 16 M. Yu, Z. Wang, C. Hou, Z. Wang, C. Liang, C. Zhao, Y. Tong, X. Lu, S. Yang, *Adv. Mater.*, 2017, **29**, 1602868.
- 17 F. Cheng, J. Chen, *Chem. Soc. Rev.*, 2012, **41**, 2172-2192.
- 18 N. S. V. Narayanan, B. V. Ashokraj, S. Sampath, J. *Electrochem. Soc.*, 2009, **156**, A863.
- 19 A. R. Mainar, E. Iruin, L. C. Colmenares, A. Kvasa, I. De Meaza, M. Bengoechea, O. Leonet, I. Boyano, Z. Zhang, J. A. Blazquez, *J. Energy Storage*, 2018, **15**, 304-328.
- 20 P. Chen, K. Zhang, D. Tang, W. Liu, F. Meng, Q. Huang, J. Liu, *Front. Chem.*, 2020, **8**, 372.
- 21 H. Miao, B. Chen, S. Li, X. Wu, Q. Wang, C. Zhang, Z. Sun, H. Li, *J. Power Sources*, 2020, **450**, 227653.
- 22 J. Park, M. Park, G. Nam, J.-s. Lee, J. Cho, *Adv. Mater.*, 2015, **27**, 1396-1401.
- 23 D. Chen, M. A. Hickner, *ACS Appl. Mater. Interfaces*, 2012, **4**, 5775-5781.
- 24 Y. A. Elabd, *Molecular Systems Design & Engineering* 2019, **4**, 519-530.
- 25 Z. Cao, H. Hu, M. Wu, K. Tang, T. Jiang, *J. Mater. Chem. A*, 2019, **7**, 17581-17593.
- 26 J. Fu, J. Zhang, X. Song, H. Zarrin, X. Tian, J. Qiao, L. Rasen, K. Li, Z. Chen, *Energy Environ. Sci.*, 2016, **9**, 663-670.
- 27 S. Nandi, V. M. Dhavale, S. Shalini, U. Werner-Zwanziger, H. Singh, S. Kurungot, R. Vaidhyanathan, *Adv. Mater. Interfaces*, 2015, **2**, 1500301.
- 28 R. Illathvalappil, V. M. Dhavale, S. N. Bhange, S. Kurungot, *Nanoscale*, 2017, **9**, 9009-9017.
- 29 M. T. Tsehaye, F. Alloin, C. Iojoiu, R. A. Tufa, D. Aili, P. Fischer, S. Velizarov, *J. Power Sources*, 2020, **475**, 228689.
- 30 D. J. Arnot, M. B. Lim, N. S. Bell, N. B. Schorr, R. C. Hill, A. Meyer, Y.-T. Cheng, T. N. Lambert, *Adv. Energy Mater.*, 2021, **11**, 2101594.
- 31 Y. Kim, M. Künzel, D. Steinle, X. Dong, G.-T. Kim, A. Varzi, S. Passerini, *Energy Environ. Sci.*, 2022, **15**, 2610-2618.
- 32 Y. Zeng, P. Gordiichuk, T. Ichihara, G. Zhang, E. Sandoz-Rosado, E. D. Wetzal, J. Tresback, J. Yang, D. Kozawa, Z. Yang, *Nature*, 2022, **602**, 91-95.
- 33 A. P. Katsoulidis, M. G. Kanatzidis, *Chem. Mater.*, 2011, **23**, 1818-1824.
- 34 R. Paul, S. C. Shit, T. Fovanna, D. Ferri, B. Srinivasa Rao, G. T. K. K. Gunasooriya, D. Q. Dao, Q. V. Le, I. Shown, M. P. Sherburne, Q. T. Trinh, J. Mondal, *ACS Appl. Mater. Interfaces*, 2020, **12**, 50550-50565.
- 35 R. Dawson, E. Stöckel, J. R. Holst, D. J. Adams, A. I. Cooper, *Energy Environ. Sci.*, 2011, **4**, 4239-4245.
- 36 B. Li, R. Gong, W. Wang, X. Huang, W. Zhang, H. Li, C. Hu, B. Tan, *Macromolecules*, 2011, **44**, 2410-2414.
- 37 S. Nandi, U. Werner-Zwanziger, R. Vaidhyanathan, *J. Mater. Chem. A*, 2015, **3**, 21116-21122.
- 38 D. Chakraborty, S. Nandi, R. Kushwaha, D. Kaleeswaran, R. Vaidhyanathan, *Mater. Res. Bull.*, 2021, **146**, 111614.
- 39 D. Crespy, M. Bozonnet, M. Meier, *Angew. Chem. Int. Ed.*, 2008, **47**, 3322-3328.
- 40 E. Breitmaier, W. Voelter, *Carbon-13 NMR spectroscopy*, VCH Publishers Inc, United States, 1987, **26**, 351.
- 41 S. Haldar, D. Rase, P. Shekhar, C. Jain, C. P. Vinod, E. Zhang, L. Shupletsov, S. Kaskel, R. Vaidhyanathan *Adv. Energy Mater.*, 2022, **12**, 2200754
- 42 L. Feng, X. Zhang, C. Wang, X. Li, Y. Zhao, X. Xie, Y. Lv, *Int. J. Hydrog. Energy*, 2016, **41**, 16135-16141.
- 43 G. A. Ludueña, T. D. Kühne, D. Sebastiani, *Chem. Mater.*, 2011, **23**, 1424-1429.
- 44 D. W. Kang, M. Kang, H. Yun, H. Park, C. S. Hong, *Adv. Funct. Mater.*, 2021, **31**, 2100083.
- 45 U. Tröltzsch, O. Kanoun, *Electrochimica Acta*, 2012, **75**, 347-356.
- 46 J. Chen, P. Li, N. Zhang, S. Tang, *J. Mater. Chem. A*, 2022, **10**, 7146-7154
- 47 S. H. Lee, J. C. Rasaiah, *J. Chem. Phys.*, 2013, **139**, 124507.
- 48 R. Vedalakshmi, V. Saraswathy, H.-W. Song, N. Palaniswamy, *Corros. Sci.* 2009, **51**, 1299-1307.
- 49 H. Zhang, B. Zhang, Y. Yang, D. Ye, R. Chen, Q. Liao, X. Zhu, *ChemComm*, 2021, **57**, 1258-1261.
- 50 Z.-L. Wang, D. Xu, J.-J. Xu, X.-B. Zhang, *Chem. Soc., Rev.* 2014, **43**, 7746-7786.
- 51 V. Dubey, S. Daschakraborty, *J. Phys. Chem. B*, 2022, **126**, 2430-2440.
- 52 J. Chen, P. Li, N. Zhang, S. Tang, *J. Mater. Chem. A*, 2022, **10**, 7146-7154.
- 53 P. Prakash, A. Shylendran, B. Fall, M. J. Zdilla, S. L. Wunder, A. Venkatnathan, *J. Phys. Chem. C*, 2022, **126**, 4744-4750.
- 54 T. Zelovich, L. Vogt-Maranto, C. Simari, I. Nicotera, M. A. Hickner, S. J. Paddison, C. Bae, D. R. Dekel, M. E. Tuckerman, *Chem. Mater.* 2022, **34**, 2133-2145.
- 55 C. Chandana, H. D. Singh, L. S. Leo, P. Shekhar, D. Rase, D. Chakraborty, C. P. Vinod, R. Vaidhyanathan. *J. Mater. Chem. A*, 2022, **10**, 15647-15656
- 56 P. Prakash, J. Aguirre, M. M. Van Vliet, P. R. Chinnam, D. A. Dikin, M. J. Zdilla, S. L. Wunder, A. Venkatnathan, *J. Mater. Chem. A*, 2018, **6**, 4394-4404.